frontiers | Frontiers in Earth Science

TYPE Original Research
PUBLISHED 21 September 2022
DOI 10.3389/feart.2022.869567

OPEN ACCESS

EDITED BY
Brian W. Romans,
Virginia Tech, United States

REVIEWED BY
Vincent Clementi,
The State University of New Jersey, United States
Justin Dodd,
Northern Illinois University, United States

*CORRESPONDENCE
Clara Sena,
clara.sena@geo.uio.no

SPECIALTY SECTION
This article was submitted to Sedimentology, Stratigraphy and Diagenesis, a section of the journal Frontiers in Earth Science

RECEIVED 04 February 2022
ACCEPTED 15 August 2022
PUBLISHED 21 September 2022

CITATION
Sena C, Parkhurst DL, Tepley III FJ, Jiang F, van der Land C, Coelho FJRC, Oliveira V, Lever MA, Ishizuka O and Arculus R (2022), Formation of calcium chloride brines in volcaniclastic-rich sediments.
Front. Earth Sci. 10:869567.
doi: 10.3389/feart.2022.869567

Formation of calcium chloride brines in volcaniclastic-rich sediments

Clara Sena[1,2]*, David L. Parkhurst[3], Frank J. Tepley III[4], Fuqing Jiang[5], Cees van der Land[6], Francisco JRC Coelho[7], Vanessa Oliveira[7], Mark A. Lever[8], Osamu Ishizuka[9,10] and Richard Arculus[11]

[1]Department of Geosciences, University of Oslo, Geologibygningen, Oslo, Norway, [2]Department of Geology and Centre for Environmental and Marine Studies (CESAM), University of Aveiro, Campus Universitário de Santiago, Aveiro, Portugal, [3]Independent Researcher, Lakewood, CO, United States, [4]College of Earth, Ocean, and Atmospheric Sciences, Oregon State University, Corvallis, OR, United States, [5]Institute of Oceanology, Chinese Academy of Sciences, Qingdao, China, [6]School of Natural and Environmental Sciences, Newcastle University, Newcastle Upon Tyne, United Kingdom, [7]CESAM—Centre for Environmental and Marine Studies, Department of Biology, University of Aveiro, Aveiro, Portugal, [8]ETH Zurich, Institute of Biogeochemistry and Pollutant Dynamics, Zurich, Switzerland, [9]Geological Survey of Japan/AIST, Tsukuba, Japan, [10]Research and Development Centre for Ocean Drilling Science, Japan Agency for Marine-Earth Science and Technology, Yokosuka, Japan, [11]Research School of Earth Sciences, Australian National University, Canberra, ACT, Australia

The Amami-Sankaku Basin, located in the Philippine Sea, records approximately 50 million years of sediment accumulation and diagenesis of volcanic ash derived from the Kyushu-Palau and Kyushu-Ryukyu arcs. Analyses of porewater and sediment samples from the 1461-m core recovered at IODP Expedition 351, Site U1438, included major and trace elements, strontium radiogenic isotope ratio ($^{87}Sr/^{86}Sr$), and taxonomic identification of archaeal classes and bacterial orders. Sediment X-ray diffraction and thin section analyses show that smectite, zeolites and chlorite are the main authigenic minerals. A multicomponent solute diffusion and reaction numerical model was developed to simulate the long-term diagenesis that took place in this sedimentary sequence and to account for the transition to a calcium chloride brine at about 670 mbsf. Numerical results indicate that 45% of the initial amount of volcanic ash has been dissolved at 750 mbsf. At this depth, 13% of the initial water (H_2O) in the pore space is estimated to have been transferred to the solid phase by the formation of zeolites, which accounts for an increase in porewater chloride concentration. In contrast, dissolution of anorthite and volcanic ash combined with sodium uptake by zeolites accounts for the predominance of calcium in the brine. In the upper 160 m of the sedimentary column, the electrochemical migration of solutes causes chloride to move in the opposite direction of the concentration gradient, i.e., uphill diffusion, sustaining downward diffusion of seawater chloride into the sediments.

KEYWORDS

volcanic ash, zeolites, electrochemical migration, reaction-diffusion model, PHREEQC, deep-sea oligotrophic prokaryotes

Introduction

According to Hardie (1983), a calcium chloride ($CaCl_2$) brine can be defined as an aqueous solution in which the double of the molality of calcium is higher than the sum of the molality of bicarbonate and the double of the molality of carbonate and sulphate, i.e.:

$$2m_{Ca^{2+}} > m_{HCO_3^-} + 2m_{CO_3^{2-}} + 2m_{SO_4^{2-}}$$

where m stands for the molality of each aqueous species (i.e., moles per kilogram of solution). Other authors such as Carpenter (1978) define a brine as an aqueous solution with more than 100,000 mg/L of total dissolved solids. In our work, we use the definition by Hardie (1983) to refer to $CaCl_2$ brines. These brines occur in a wide variety of geological settings, including saline lakes (Katz and Starinsky, 2008); volcanic or sub-volcanic geothermal provinces (Lowenstein and Risacher, 2008); submarine hydrothermal vents associated to rift zones (Hardie, 1983); oil fields (Gavrieli et al., 1995); and, volcaniclastic-rich sediments with abundant hydrated authigenic minerals (Egeberg et al., 1990; Martin, 1994; Blanc et al., 1995). Different biogeochemical, solute transport and evaporation processes lead to the formation of the $CaCl_2$ brines found in this wide range of geological settings. In this paper, we focus our attention to the formation of $CaCl_2$ brines in volcaniclastic-rich sediments because their nature is still not fully understood.

In the Izu-Bonin fore-arc basin, located in the northeast Philippine Sea Plate, Egeberg et al. (1990) reported highly-enriched $CaCl_2$ brines at depths below 850 mbsf (meters below seafloor) in a volcaniclastic-rich sedimentary sequence. According to these authors, the strongest porewater geochemical changes coincide with the Miocene/Oligocene boundary and include a pH increase from 7.6 to 8.9, magnesium and potassium concentrations decreasing towards zero, calcium becoming the dominant dissolved cation at the expense of sodium, and an increase in chloride concentrations. In addition, where sedimentary sequences have high content of volcanic ash porewater strontium is enriched in the lighter isotope ^{86}Sr compared to contemporaneous seawater (Aagaard et al., 1989; Blanc et al., 1995). A similar geochemical evolution of the porewaters, and the occurrence of a $CaCl_2$ brine at depth, have been reported at the Aoba Basin, in the New Hebrides convergent margin (Martin, 1994).

The main processes responsible for this deep evolution in porewater geochemistry have been identified as 1) dissolution of primary minerals, including those in the underlying igneous crust, and volcanic ash accumulated in sedimentary layers; 2) precipitation of authigenic zeolites and clays; and, 3) solute diffusion in the water-filled pore space (McDuff and Gieskes, 1976; Gieskes and Lawrence, 1981; Aagaard et al., 1989; Blanc et al., 1995; Lee and Klein, 2003).

Volcanic ash deposited in deep-sea sedimentary basins becomes thermodynamically unstable in contact with seawater and at depth in the sedimentary column as the temperature and pressure increase. Its high reactivity, even when small amounts of volcanic ash are embedded in the sediments, leads to visible changes in porewater chemistry, including an increase in calcium and chloride concentration, a decrease in the $^{87}Sr/^{86}Sr$ ratio, and a decrease in the $\delta^{18}O$ values (Gieskes & Lawrence, 1981; Martin, 1994). As a consequence of volcanic ash alteration, authigenic smectite and zeolites, such as clinoptilolite, analcime, phillipsite, and heulandite, form (Cosgrove and Papavassiliou, 1979; Tsolis-Katagas and Katagas, 1990; Vitali et al., 1995). In deep-sea sediments, Blanc et al. (1995), Egeberg et al. (1990) and Martin (1994) argue that the increase in porewater chloride with sediment depth is due to the transfer of H_2O from porewater into the solid phase, when hydrous minerals, such as smectite and zeolites, form.

A second possible mechanism for the increase in porewater chloride concentrations is pressure-driven filtration through a semi-permeable membrane, also known as reverse osmosis, which allows solvent water to pass easily through the membrane, and hinders the passage of dissolved ions (Egeberg et al., 1990; Gieskes, et al., 1990; Blanc et al., 1995). This process has often been attributed to the presence of clay-rich units in sedimentary basins, located deep enough to experience high compaction pressures. When dissolved ions such as chloride experience pressure-driven filtration, a low concentration of these ions should be observed at the low pressure side of the semi-permeable membrane (Hanshaw and Coplen, 1973; Kharaka and Berry, 1973; Martin et al., 1995).

The electrochemical migration of chloride is hypothesised here as a third possible process for the increased chloride concentration in volcanic ash-rich oligotrophic sediments. Electrochemical migration is the movement of charged ions in a multicomponent aqueous solution to maintain charge balance when ions diffuse at different rates. This process can be especially important in diffusion-dominated settings that are common in deep-sea sedimentary basins (Boudreau et al., 2004; Rasouli et al., 2015; Sprocati et al., 2019). In order to test this hypothesis, we develop a multicomponent diffusion and reaction numerical model with PHREEQC version 3.7.1 (Parkhurst and Appelo, 2013) that simulates 48.7 million years of sediment accumulation and volcanic ash diagenesis in the Amami-Sankaku Basin (ASB), in the north Philippine Sea. This numerical model is constrained by geochemical, isotopic, mineralogical and microbiological data produced from the International Ocean Discovery Program (IODP) Site U1438; Arculus et al. (2015a).

Besides inorganic mineral-water interactions, biologically driven redox reactions can also influence the chemical composition of deep-sea porewater sediments. Previous

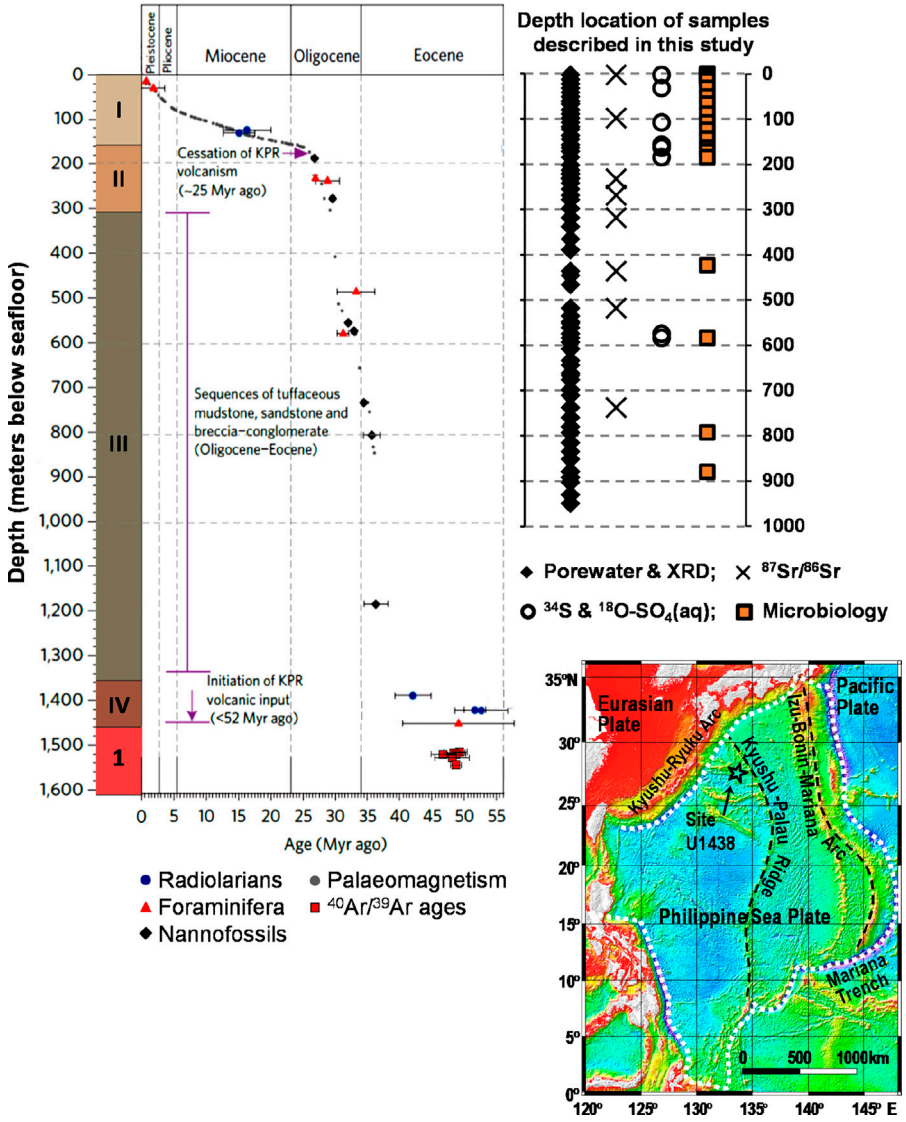

FIGURE 1
Lithostratigraphy of IODP Site U1438 and depth location of the samples described in this study. Lithostratigraphic units described in the main text. Insert is a bathymetric map with location of Site U1438 (red < 100 m, purple > 10,000 m). Image with age-depth model modified from Arculus et al. (2015b). Radiometric ($^{40}Ar/^{39}Ar$) ages of the oceanic crust from Ishizuka et al. (2018).

studies demonstrate that in deep-sea oligotrophic sediments, prokaryotic activity is associated to geochemical and sedimentary interfaces over geological timescales, catalysing water-rock interactions with redox sensitive elements such as sulphur, manganese, iron, carbon and nitrogen (D'Hondt et al., 2004; Parkes et al., 2005). For these reasons, in addition to the inorganic geochemical and physical processes that lead to the formation of a $CaCl_2$ brine in the ASB we focus on the prokaryotic activity and their implications for the water-rock interactions in the sediments deposited here.

Materials and methods

In 2014, a 1,461 m-thick volcaniclastic-rich sequence was recovered from the International Ocean Discovery Program (IODP) Site U1438 in the ASB (27°23.0′N, 134°19.1′E), on the northern Philippine Sea Plate, using the R/V *JOIDES Resolution* (Figure 1). A convergent margin, where the Pacific Plate subducts beneath the Philippine Sea Plate, is located 900 km east of Site U1438. The ASB is a trench-distal, former rear-arc basin of a previously (~45–25 Ma) active island arc–now comprising the Kyushu-Palau Ridge (KPR). The Philippine Sea Plate subducts

TABLE 1 Description of the lithostratigraphic units defined at IODP Expedition 351, Stie U1438 (Arculus et al., 2015a), and average sedimentation rate as depicted from Figure 1.

Lithostratigraphic unit	Depth range (mbsf)	Lithology	Average sedimentation rate (m/Ma)
I	0–160.3	Unconsolidated terrigenous, biogenic, and volcaniclastic fine sediments	9
II	160.3–309.6	Semi-consolidated tuffaceous mudstone, siltstone, and fine sandstone	30
III	309.6–1,361.4	Consolidated tuffaceous mudstone to coarse sandstone and tuffaceous breccia-conglomerate (Johnson et al., 2021)	240
IV	1,361.4–1,461.1	Consolidated radiolarian-bearing mudstone (Waldman et al., 2021)	30
1		Igneous basement comprising lava flows composed of sparsely vesicular, microcrystalline to fine-grained, aphyric to sparsely porphyritic, low-K-Ti tholeiitic basalt (Kusano et al., 2021; Li et al., 2021)	

beneath the Kyushu-Ryukyu arc 500 km Northwest of Site U1438. Volcaniclastic debris and ash erupted from the KPR (Brandl et al., 2017; McCarthy et al., 2021), and currently active Izu-Bonin-Mariana and Kyushu-Ryukyu arcs (McCarthy et al., 2019) respectively, has accumulated in the ASB and now lies at a water depth of 4,700 m in the Philippine Sea (Arculus et al., 2015a; Ishizuka et al., 2018).

The volcaniclastic sequence recovered in Site U1438 was divided into four lithostratigraphic units and one additional unit comprising the underlying oceanic crust. The five units can be summarized from top to bottom as presented in Table 1. The paleobathymetry of Site U1438 was assessed in Arculus et al. (2015a) and ranges from bathyal to abyssal depths, i.e., from 1,000 to > 4,000 m of water depth throughout the history of the ASB. This indicates that the sediments deposited here were not under shallow enough conditions to allow for the formation of brines as a consequence of evaporation in a closed basin. This process can, therefore, be discarded in the ASB, and the $CaCl_2$ brine observed in this basin can be addressed as a consequence of the long-term water-rock interactions that modified the original composition of seawater under deep-sea conditions.

A total of 66 porewater samples and 25 sediment samples for microbiological analyses were taken to a depth of 950 mbsf (Figure 1). The deepest porewater samples collected in all holes drilled in the Ocean Drilling Program (ODP; 1985–2003), International Ocean Drilling Program (IODP; 2003–2013) and, International Ocean Discovery Program (IODP; 2013–2019) have an average depth of 188 mbsf, and only 2.5% of these porewater samples reach depths higher than 770 mbsf. Therefore, the porewater samples recovered at Site U1438 are among the deepest to date in deep-sea oligotrophic sediments, and allowed us to investigate relationships between deep porewater compositions, microbiological abundance and diversity.

Chemical analyses of porewater samples and X-ray diffraction (XRD) analyses of sediments were completed aboard the R/V *JOIDES Resolution*. Porewater was extracted by squeezing 66 sediment samples. For this purpose, a whole-round core sample was collected immediately after core sectioning on deck, and taken to the onboard geochemistry laboratory where the sediment sample was squeezed, and the interstitial porewater collected and analysed for salinity, pH, alkalinity, and major and minor elements. Porewater salinity was measured with a temperature-compensated handheld refractometer (Fisher Model S66366), pH was measured with a combination glass electrode, and alkalinity was determined by Gran titration with an autotitrator (Metrohm 794 basic Titrino). The concentration of porewater ammonium and phosphate was determined on an Agilent Technologies Cary Series 100 UV-Vis spectrophotometer while chloride and sulphate were analysed on a Metrohm 850 Professional II ion chromatograph. The concentration of sodium, potassium, magnesium, calcium, aluminium, manganese, iron, strontium, barium and silica in the porewater samples was analysed in a high-precision inductively coupled plasma atomic emission spectrometer (ICP-AES) by Teledyne Leeman Labs Prodigy (further details in Arculus et al., 2015b; Gieskes et al., 1991; Murray et al., 2000).

The sediment samples left after squeezing for extraction of the porewater samples were freeze-dried for 12 h and then analysed onboard for XRD using the Bruker D4 Endeavor X-ray diffractometer with a generator voltage of 35 kV and current of 40 mA. Continuous scans were collected from 4° to 75° 2θ for 4,276 steps at a rate of 1 s/step. The corresponding XRD raw files containing the diffractogram of each sediment sample were interpreted by using the software Profex version 4.3.2a (Döbelin, 2021). The relative abundance of (amorphous) volcanic ash was estimated aboard the *JOIDES Resolution* based on smear-slide and thin-section microscopic analysis and interpretation.

Methane headspace analyses were conducted aboard the JOIDES resolution approximately every 10 m. For this purpose, a 5 cm^3 sediment sample was collected from the core immediately after sectioning on deck, placed in a 20 cm^3 glass vial, and sealed with a Teflon/silicon septum and a crimped aluminium cap. A 5 cm^3 aliquot of the evolved hydrocarbon gases was extracted from the headspace vial with a standard gas

syringe and then manually injected into an Agilent/Hewlett Packard 6,890 Series II gas chromatograph equipped with a flame ionization detector set at 250°C. The results, reported as parts per million volume (ppmv), were collected using the Hewlett Packard 3,365 ChemStation data processing software (Arculus et al., 2015b).

Strontium isotopic analyses ($^{87}Sr/^{86}Sr$) of porewater and bulk sediment samples were completed by Thermal Ionization Mass Spectrometry (TIMS), at the University of Aveiro. The relative abundance of stable isotopes of sulphur and oxygen ($\delta^{34}S$ and $\delta^{18}O$) were analysed in aqueous sulphate from selected porewater samples by Isotope Ratio Mass Spectrometry (IRMS), at the University of Salamanca. Further details regarding sample preparation and analytical methods are given in sections 1 and 2 of Supplementary Material S1, respectively.

Collected ash samples were water-sieved at the 63–125 μM size fraction to remove any surrounding clay or sand matrix if present. The samples were analysed for major and minor element compositions using a CAMECA SX-100 electron microprobe, at Oregon State University.

For microbiological analyses, approximately 30 cm^3 of sediment were collected with a sterilized minicorer for quantitative PCR (qPCR) and high-throughput DNA sequencing. All samples were stored and shipped frozen at −80°C (more details in Arculus et al., 2015b). DNA was extracted from all sediment samples following Lysis Protocol II in Lever et al. (2015). Total numbers of 16S rRNA gene copies were quantified with qPCR and a 16S rRNA gene based high-throughput sequencing approach was used for the characterization of bacterial and archaeal communities. Detail information can be found in section 4 of the Supplementary Material S1. The sequence reads obtained in this study are available in the National Center for Biotechnology Information (NCBI) under accession number PRJNA753247.

The PHREEQC version 3.7.1 (Parkhurst and Appelo, 2013) is a numerical modelling code that calculates aqueous speciation, equilibrium and/or kinetically controlled geochemical heterogeneous reactions and transport of solutes in multicomponent aqueous solutions (i.e., electrochemical migration of solutes) for ionic strengths up to seawater and above. For thermodynamic equilibrium calculations, PHREEQC is oriented toward system equilibrium (i.e., solvent water, dissolved species, gaseous and solid phases) rather than just aqueous equilibrium (dissolved species, gaseous and solid phases), and therefore, all moles of each element in the system, including the moles of hydrogen and oxygen in solvent water (which are crucial to quantify the removal of H_2O from the pore space when hydrous minerals form), are distributed among aqueous and solid phases. The effect of pressure, temperature and ionic strength on the volume of aqueous species and mineral solubility are also calculated in PHREEQC. For these reasons, PHREEQC version 3.7.1 was used to perform a sequence of tasks culminating with the development of a one-dimensional reaction-diffusion model simulating prolonged volcanic ash diagenesis at IODP Site U1438. These tasks are summarized as (additional details are given in Supplementary Material S2):

1) Aqueous speciation of the collected porewater samples and calculation of the saturation indices (SI) of these porewaters with respect to the main primary (feldspars, olivine, pyroxenes and quartz) and secondary minerals (zeolites, clays, calcium carbonates and sulphates). The molality of carbonate (CO_3^{2-}) and bicarbonate (HCO_3^-) ions was also obtained in this aqueous speciation, for assessing the presence of a $CaCl_2$ brine according to the definition by Hardie (1983).
2) 1D reaction-diffusion model that simulates 48.7 million years of volcanic ash diagenesis at the IODP Site U1438. This model allowed us to numerically couple (i) the accumulation of sediments at the sedimentation rates depicted in Figure 1; (ii) the dissolution of primary minerals and volcanic ash and precipitation of secondary minerals; and, (iii) the multicomponent diffusion of dissolved species through the porous space in the accumulated sediments and volcanic ash.

The build-up of the sedimentary column and its diagenetic processes at the ASB can be seen as a one-dimensional (1D) vertical accumulation of sediments rich in volcanic ash and minerals. In this context, the 47.8 Ma-duration of sediment accumulation history in the ASB was simulated by running twenty sequential 1D reaction-diffusion simulations (Figure 2). Starting with 1 cell, and subsequently adding a cell at the top of the previous simulation, so that the final 1D column is made of 20 cells representing the ~1,460 m-thick sedimentary sequence of the ASB. The values of the thickness and sediment porosity of each cell added to the numerical model were defined based on the observed sedimentation rate and the discrete shipboard porosity measurements (Arculus et al., 2015a).

The chemical composition of the volcanic ash reflects the rhyolitic composition of the magmatic source of the volcaniclastics deposited in the ASB. For this reason, we selected volcanic ash and anorthite as the only primary reactive solid phases modelled with kinetic constraints, with an initial amount of 25 and 10 wt%, respectively (corresponding to the *unreacted minerals* in Figure 2). The kinetic rate equations implemented for the dissolution of volcanic ash and anorthite were compiled by Palandri and Kharaka (2004). These authors compiled rate equations conforming to a general Arrhenius-type rate equation for over 70 minerals, including anorthite and amorphous silica (the latter implemented in our model as a proxy for volcanic ash). The porewater composition implemented as the *unreacted porewater* and as *constant water chemistry* at the top boundary of the numerical model, shown in Figure 2, corresponds to the porewater composition measured at the shallowest sample collected (at 3 mbsf) at IODP Site U1438.

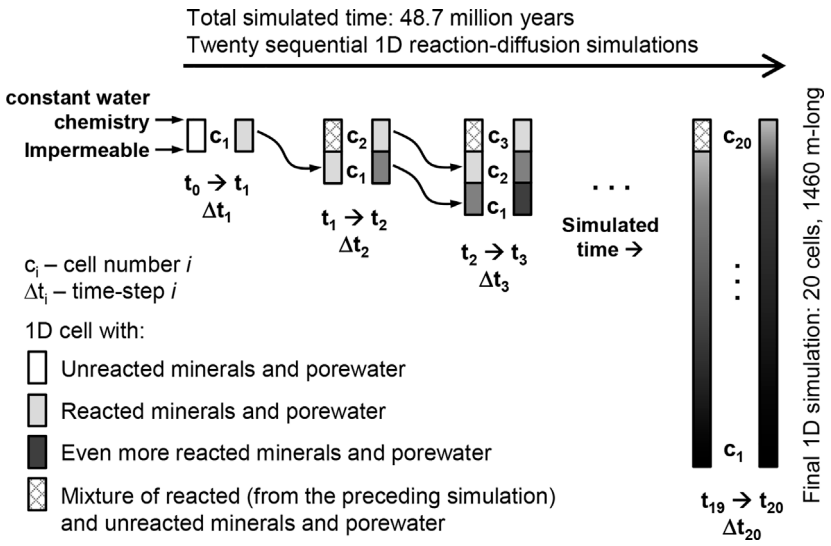

FIGURE 2
Illustration of the methodology implemented in PHREEQC for simulating the build-up of the sedimentary column, geochemical reactions and solute diffusion in the Amami-Sankaku Basin for 48.7 Ma. The boundary conditions are constant at the top of the column and closed at the bottom of the column for the twenty reaction-diffusion simulations.

More details are given in section 1.2.1 of Supplementary Material S2.

Based on thin-section, smear-slide and XRD analyses and interpretations performed aboard the *JOIDES Resolution* (Arculus et al., 2015a), and the post-cruise XRD interpretation performed in this work, chlorite, calcite, amorphous silica, pyrite, anhydrite, barite, hematite, smectite, manganese oxyhydroxides, and rhodochrosite are modelled as secondary minerals, treated as equilibrium phases that are allowed to precipitate if they become saturated. Clinoptilolite and montmorillonite are modelled as linear solid solutions to accommodate for the different cations that can be present in these authigenic minerals. For clinoptilolite, the end-members with Na, K, Sr and Ba are considered, while for montmorillonite the end-members with Ca and K are considered.

To better represent the observed porewater composition in the ASB, the 1D reaction-diffusion numerical model was calibrated for two kinetic rate parameters–the specific surface area of volcanic ash and anorthite–and five equilibrium constants–the solubility constant of the authigenic mineral phases amorphous silica, Na-clinoptilolite, K-clinoptilolite, Ba-clinoptilolite, and Sr-clinoptilolite. This calibration was done automatically by using PEST (Doherty, 2005) to match measured porewater data (pH, chloride, sulphate, dissolved inorganic carbon (calculated from the measured alkalinity, using PHREEQC), silica, sodium, calcium, magnesium, potassium, barium, and strontium) with numerically computed porewater data. Mineralogical data were used in formulating the reaction processes, but no quantitative mineralogy was used in the model calibration (more details are given in section 1.2.2 of Supplementary Material S2).

Results

Porewater chemistry

Onboard petrophysical analyses, and borehole temperature readings of the sedimentary sequence recovered in Site U1438 indicate a geothermal gradient of 77.7°C/km. Therefore, the *in-situ* temperature ranged from 1.7°C for the shallowest porewater sample to 75.2°C for the deepest sample (at 3 and 949 mbsf, respectively). From the seafloor to the deepest porewater, the sediment porosity decreases from 75 to 34% (Arculus et al., 2015a). Based on these physical properties, the *in-situ* temperature and hydrostatic pressure of each porewater sample were calculated (section 1, in Supplementary Material S2) and their depth relationship was used to specify the temperatures and pressures of cells in the reaction-diffusion model (section 1.2.1, in Supplementary Material S2).

From 3 to 815 mbsf, porewater chloride increases from 0.564 to 0.683 mol/kgw (mole per kilogram of water), corresponding to a 1.2-fold increase (Figure 3). A chloride minimum is registered at 145 mbsf, located 15 m above the lithostratigraphic boundary between Units I and II (the Miocene/Oligocene transition). Similar minima are observed in the sodium, sulphate, Total Dissolved Solids (TDS, shown in

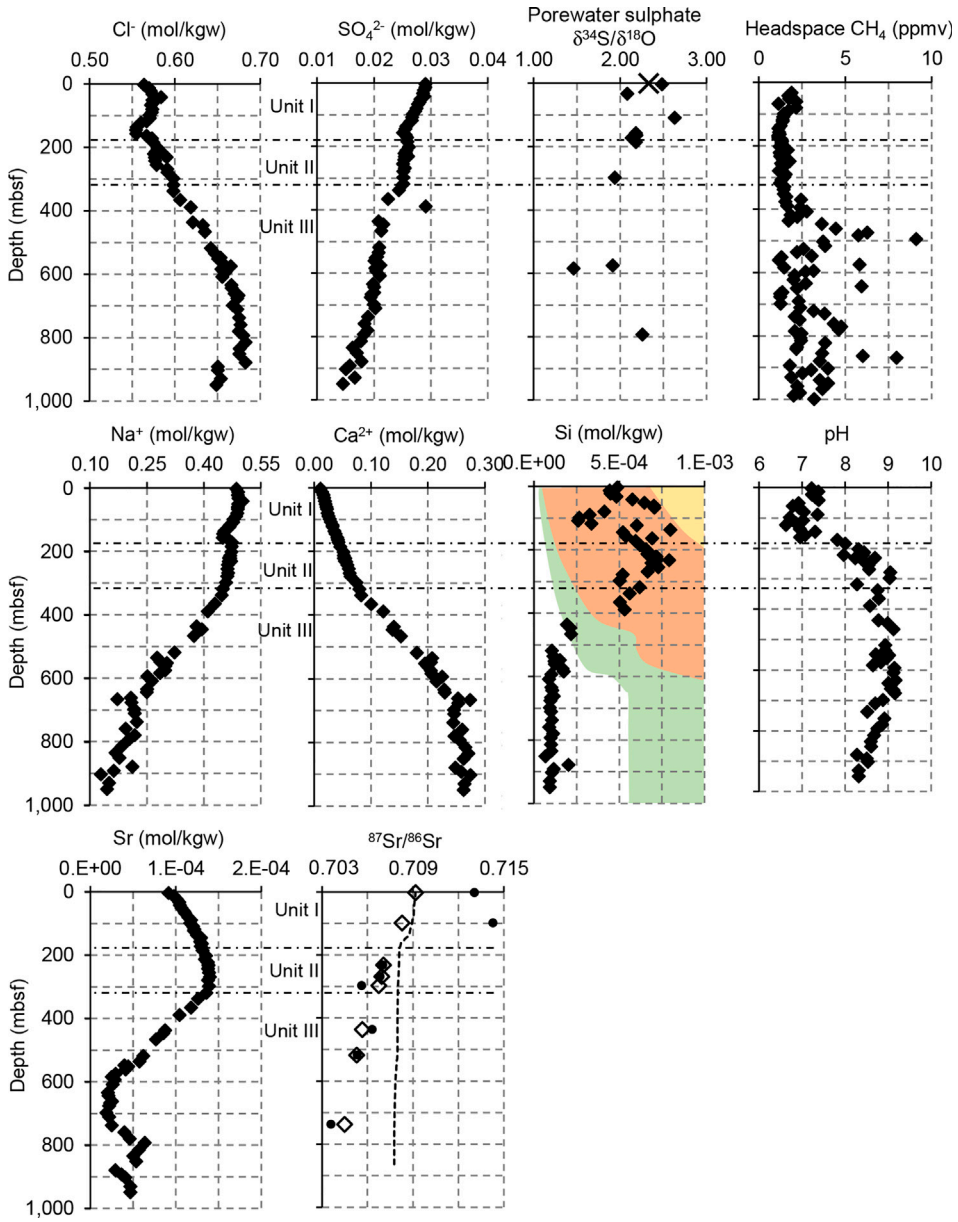

FIGURE 3
Observed porewater depth profiles of chloride, sulphate, sulphate $\delta^{34}S$ and $\delta^{18}O$ ratio (seawater ratio at sea-level is shown with a cross at the top of the plot), headspace methane (CH_4), sodium, calcium, silica, pH, strontium; and, $^{87}Sr/^{86}Sr$ in porewater (open diamonds), bulk sediment (black dots), and contemporary global seawater (semi-vertical dashed line anchored at seafloor as ~ 0.709, calculated from McArthur et al., 2001). The stability fields of amorphous silica (yellow), α-cristobalite (orange), and quartz (green) calculated with PHREEQC are shown in the plot with observed porewater silica.

Figure 6) and pH depth profiles. Porewater strontium and calcium do not show minima (Figure 3).

The smooth linear downward decrease in porewater sulphate, the extremely low headspace methane concentrations (below 10 ppmv), the low rate of sulphate-reducing bacterial activity indicated by the observed range of $\delta^{34}S_{CDT}$ (20.6–24.0 ±0.35‰, given in section 2 of the Supplementary Material S2, and the trend of the porewater sulphate $\delta^{34}S/\delta^{18}O$ indicate that the methane-sulphate redox transition was not reached at IODP Site U1438 (Figure 3).

Porewater calcium increases with depth from 0.012 to 0.275 mol/kgw, while sodium decreases from 0.501 to 0.128 mol/kgw. This corresponds to a 23-fold increase for calcium and a 0.26-fold decrease for sodium. At 666 mbsf,

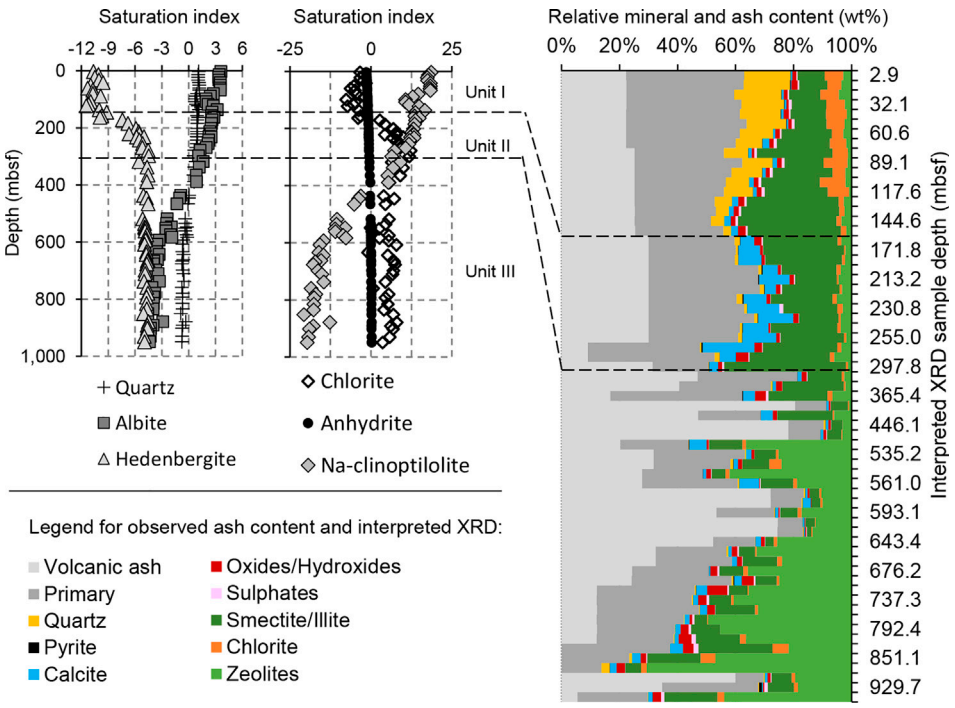

FIGURE 4
Calculated Saturation Indices (SI) of the porewaters with respect to selected primary (quartz, albite, and hedenbergite) and secondary minerals (Na-clinoptilolite, chlorite (clinochlore 14A), and anhydrite), observed volcanic ash content, and mineral abundance estimated from the XRD, corrected for the content of ash. XRD legend: "Primary" includes albite, anorthite, orthoclase, sanidine, microcline, muscovite, jadeite, diopside, enstatite, and fayalite; "Oxides/Hydroxides" include goethite, gibbsite, hausmannite, pyrolusite, and brucite; "Zeolites" include clinoptilolite, heulandite, laumontite, and analcime; "Sulphates" include anhydrite and barite.

calcium becomes the dominant cation at the expense of sodium, magnesium and potassium, and, according to the definition by Hardie (1983), a $CaCl_2$ brine is observed in the ASB from this depth downwards.

Porewater silica has many inflections in Units I and II with a maximum of 8.0×10^{-4} mol/kg at the bottom of Unit I and top of Unit II, coinciding with the Miocene/Oligocene transition. The aqueous speciation calculations performed with PHREEQC (detailed in section 1, in Supplementary Material S2) indicate that quartz and α-cristobalite are the most stable silica-solid phases for the measured porewater chemistry, pressure and temperature conditions until 500 mbsf (Figure 3). The pH is around 7 in Unit I, and increases abruptly in Unit II to 9.0. This value is sustained in Unit III until 676 mbsf, below which pH decreases to 8.3.

Porewater strontium reaches a maximum of 1.4 mol/kgw × 10^{-4} mol/kgw at 267 mbsf, in Unit II, and a minimum of 2.0 mol/kgw × 10^{-5} mol/kgw at 698 mbsf, in Unit III. The ratio of porewater strontium isotopes, $^{87}Sr/^{86}Sr$, decreases with depth roughly linearly from 0.7092 to 0.7045. Except for the shallowest porewater sample, all the others show a considerable deviation from the contemporary seawater $^{87}Sr/^{86}Sr$ (Figure 3). The majority of the porewaters are in the interval between the bulk sediment and the contemporary seawater $^{87}Sr/^{86}Sr$, and most samples below 200 mbsf are close to the bulk sediment signature. Only two samples (at 98 and 436 mbsf) are clearly out of this interval, likely indicating diffusion of porewater strontium from deeper parts of the ASB where the isotopic composition of strontium is lighter and less influenced by continental radiogenic ^{87}Sr. As Hawkesworth and Elderfield (1978) found in the Madagascar Basin and the Iceland-Faeroe Ridge, volcanic minerals, volcanic ash and the basaltic lava flows that form the basement of deep-sea sedimentary basins are characterized by a relatively light isotopic composition of strontium, and their dissolution contributes to low values of $^{87}Sr/^{86}Sr$ in the porewater.

Volcanic ash composition and sediment mineralogy

Smear-slide and thin-section microscopic analysis and interpretation conducted aboard the R/V *JOIDES Resolution* reveal a volcanic ash content, that is, on average 24, 27, and 36 wt% in Units I, II and III, respectively (Figure 4). The XRD-estimated amount of primary volcanic minerals is on average 35, 33 and 24 wt% in Units I, II and III, respectively, where albite,

TABLE 2 Electron microprobe analytical data obtained at Oregon State University for the volcanic ash sample collected at 111.9 mbsf, at IODP Site U1438. The full sample reference is U1438B-13H-1; 66 cm. The data is given in molar ratios of each chemical element. This dataset is used to define the chemical composition of the volcanic ash implemented in the numerical model developed with PHREEQC.

Sample reference	Si	Al	Na	Mg	Ti	Cl	S	K	Ca	Mn	Fe	P	O	Total
U1438B-13H-1; 66 cm	25.93	5.29	2.78	0.06	0.04	0.14	0.01	1.44	0.54	0.01	0.56	0.01	63.19	100.01

anorthite and muscovite are the dominant mineral phases ("Primary" in Figure 4).

The electron microprobe analyses conducted at Oregon State University indicate that the volcanic ash accumulated in the ASB is composed of 63% of oxygen, 26% silica, 5% of aluminium, 3% of sodium, 1% of potassium, 0.6% of iron, 0.5% of calcium, and the remaining are trace amounts of chloride, magnesium, titanium, sulphur, manganese and phosphorous (Table 2).

Downhole changes in mineralogy at Site U1438 documented from smear slide, XRD, and thin section observations show dominantly fresh volcanogenic minerals and ash present in Units I and II (depths <300 mbsf) which are transformed into mixtures of dominantly clay and zeolite minerals in Unit III (at depths >500 mbsf). These mineralogical changes can be seen as diagenetic reactions which are triggered mainly by the thermal gradient (Arculus et al., 2015a). Post-cruise complementary interpretation of the XRD data, and the quartz stability calculations performed with PHREEQC (and plotted in Figure 3), allow us to state that quartz is mainly a primary volcanic and detrital mineral in the ASB, and it is much more abundant in Unit I (16 wt% maximum) than in any other lithological unit. Illite and chlorite are mostly detrital minerals in Unit I, when this sedimentary basin received more continental inputs, and detrital/biogenic calcite is preserved in Unit II (18 wt% maximum, Figure 4).

According to smear slide, thin section and XRD shipboard analyses and interpretation, smectite and zeolites are authigenic minerals in the ASB (Arculus et al., 2015a). The complementary XRD interpretation performed now indicates that smectite is more abundant in Unit II (42 wt% maximum), and zeolites are more abundant in Unit III (70 wt% maximum, Figure 4).

The PHREEQC-calculated saturation indices indicate that these silica-rich porewaters are close to equilibrium with quartz throughout the sedimentary sequence, becoming slightly undersaturated at 500 mbsf where the increased temperature affects quartz stability (Figure 3 and Figure 4). The clear undersaturation in hedenbergite in the upper 400 mbsf, reflects the high reactivity of the primary mafic minerals when in contact with seawater.

Porewaters oversaturated in albite until 400 mbsf may indicate the albitization of plagioclase, meaning that albite is not only a primary, but also a secondary mineral in the ASB. The oversaturation of the porewaters in Na-clinoptilolite (above 400 mbsf) and its presence in XRD data indicate that this is an important secondary mineral in this sedimentary basin. Chlorite is much more oversaturated in Units II and III than in Unit I, indicating that it might be an authigenic mineral in Units II and III, but not in Unit I. The porewaters are close to equilibrium with anhydrite at all depths, and XRD and thin section data obtained onboard confirm its presence.

Prokaryotic diversity and abundance

The depth distributions of bacterial and archaeal 16S rRNA gene abundances show a consistent trend (Figure 5). Bacterial 16S rRNA genes are more abundant than archaeal 16S rRNA genes in all the sampled sediments depths. Bacterial and archaeal 16S gene abundances are highest in the upper 7 m and decrease below 10 m (Figure 5).

The taxonomic analysis showed that at the sediment-water interface (topmost stacked bar in Figure 5), archaeal classes are clearly dominated by the Nitrosopumilales (98%) which was found in other deep-sea oligotrophic sediments and manganese nodules (Schauer et al., 2011; Blöthe et al., 2015). At the same depth, Rhodospirillales (32%) is the dominant bacterial order, followed by GR-WP33-30 (7%). These bacterial orders were observed by Wu et al. (2013) in deep-sea ferromanganese polymetallic nodules.

At 3 mbsf (second topmost stacked bar in Figure 5), the phylum Woesearchaeota is relatively abundant (33%), followed by the classes Thermoplasmata (8%), Nitrosopumilales and Marine Benthic Group A (both at 7% relative abundance). Thermoplasmata becomes the dominant class (higher than 80%) below 50 mbsf. This class was found associated with methane gas hydrates and pockmarks in marine sediments (Lanoil et al., 2005, among others). Methanobacteria are also relatively abundant (97%) at 90 mbsf, revealing some methanogenic activity in the ASB.

The relative abundance of the bacterial orders Sh765B-AG-111 and vadinBA26 increases with depth, reaching 39 and 22% at 67 mbsf, respectively. Durbin and Teske (2011) and Jungluth et al. (2013) found these bacterial orders in the South Pacific Gyre and in the eastern flank of the Juan de Fuca Ridge, respectively, confirming their presence in deep-sea oligotrophic sediments.

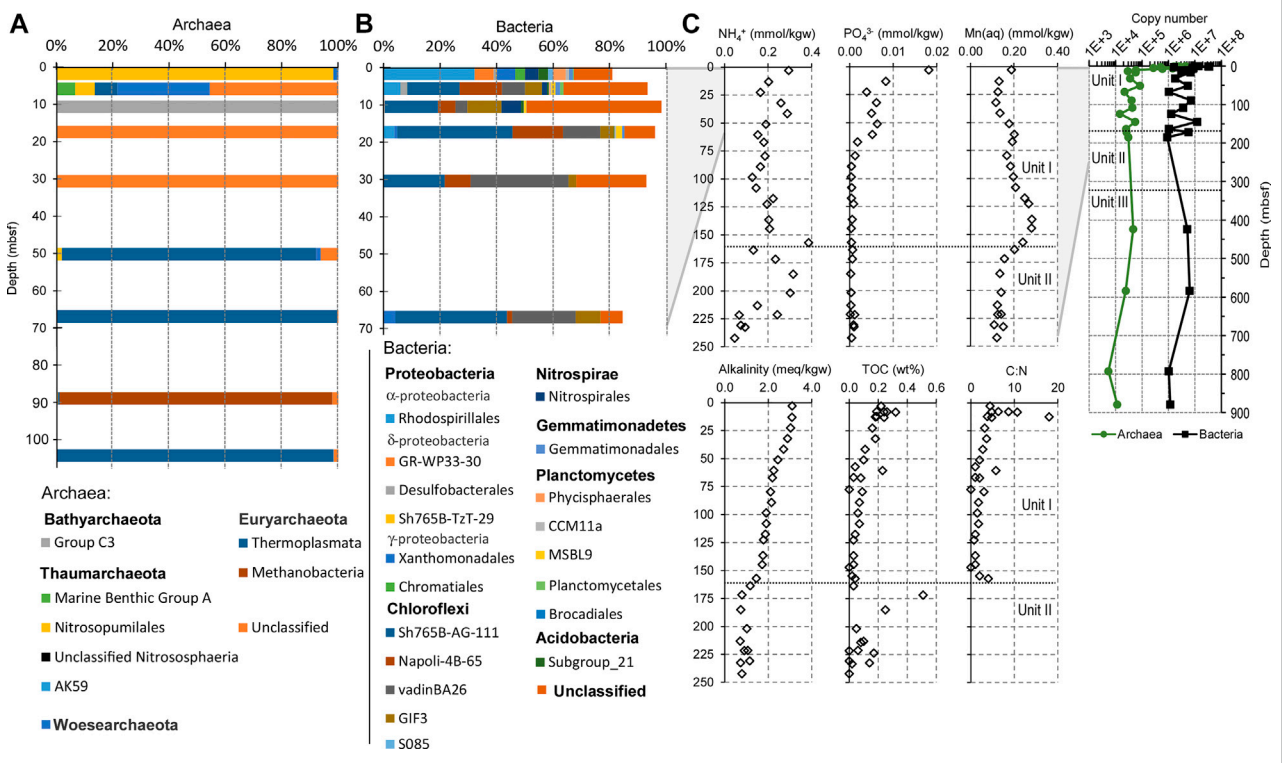

FIGURE 5
(A) Depth profiles of the relative abundance of the most abundant Archaeal groups at class level, Woesearchaeota phylum and unclassified OTUs at class level. **(B)** Depth profiles of the most abundant Bacterial groups and unclassified OTUs at order level. **(C)** Depth profile of total abundance (copy number) of Archaea and Bacteria; and selected geochemical variables. The tabular data shown in these plots is given in. tsv files (tab-separated values), in Supplementary Material S1.

In the porewater, the highest concentrations of phosphate (0.002–0.2 mmol/kgw) occur until 50 mbsf, while high ammonium concentrations (0.1–0.4 mmol/kgw) occur until 200 mbsf (Figure 5). These are important products of prokaryotic metabolic activity, and their occurrence coincides with the highest abundance of Bacteria and Archaea. The higher total organic carbon and C:N ratio observed until 60 mbsf are also in line with these findings. Just below the boundary between Units I and II, the highest TOC (0.5wt%) for the whole drilled sequence is recorded. This could be linked to the presence of an 'initial compaction window' between 83 and 113 mbsf (Maffione and Morris, 2017) acting as a low vertical permeability layer that inhibited the downward flux of oxidizing waters, and subsequent degradation of organic matter in the buried sediments.

Porewater alkalinity, with an almost linear decrease from the seafloor to the boundary between Units I and II, seems to reflect more the influence of geochemical and diffusion processes than biological processes. On the contrary, porewater manganese, with more visible inflections in Unit I, may reflect the activity of prokaryotes that use Mn(IV)-oxides (observed throughout these sediments) as an electron acceptor. The archaeal phylum Woesearchaeota, common in suboxic sediments with metal reduction, could be one of these (Liu et al., 2018).

The low organic matter content in the whole sedimentary sequence (TOC in Figure 5), and the relative low abundance of methanogenic and sulphate-reducing prokaryotes confirms the sulphate-methane transition was not reached. Therefore, the main driving forces for diagenesis in the ASB do not seem to be organic matter degradation and concomitant consumption of electron acceptors, but mostly inorganic geochemical reactions. Based on these findings, an inorganic reaction-diffusion model was developed with PHREEEQC to numerically simulate the long-term diagenesis of volcanic ash at IODP Site U1438.

PHREEQC reaction-diffusion modelling results

Saturation index calculations and mineralogical analyses make pure mineral phases containing chloride unlikely. Nonetheless, the bulk geochemical composition of the volcanic ash sampled in the ASB, shows that this anion is

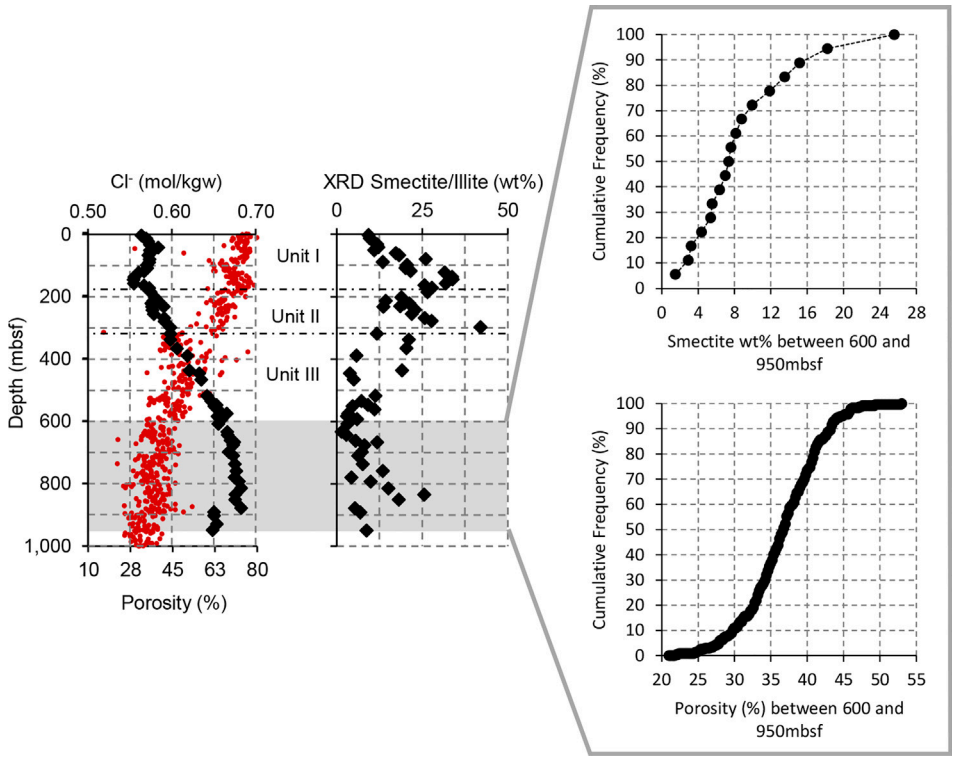

FIGURE 6
Depth profiles of observed porewater chloride (black diamonds), sediment porosity (red circles) and XRD-estimated content of smectite; and, the cumulative frequency curves of sediment porosity and XRD-estimated content of smectite for the depth interval with the highest chloride concentration—600 to 950 mbsf.

present in trace amounts, with a molar fraction of 0.0014. Therefore, the observed porewater chloride increase with depth should be the result of one or a combination of four processes: 1) ash dissolution; 2) incorporation of water (H_2O) in hydrous secondary minerals such as smectite and zeolites; 3) reverse osmosis; and, 4) electrochemical migration of chloride.

In the ASB, the highest porewater chloride concentration occurs between 600 and 950 mbsf. At this depth, the relatively high sediment porosities (70% of the sediment samples between 600 and 950 mbsf have a porosity between 34 and 53%) and low clay content (XRD data reveals 70% of the sediment samples between 600 and 950 mbsf with a clay content lower than 9 wt%) allow us to discard the hypothesis of reverse osmosis for the observed high porewater chloride (Figure 6). Therefore, we developed a 1D reaction-diffusion model with PHREEQC (Parkhurst and Appelo, 2013), with the methodology described in Figure 2, that couples the remaining three processes.

The results of the reaction-diffusion numerical model fit well the general observed trends in porewater chemistry, with the exception of silica (Figure 7). Simulated porewater chloride, calcium and TDS agree best with observations (the same is true for sodium, magnesium, and potassium, shown in Supplementary Material S2), while simulated pH, strontium and silica show larger discrepancies.

Simulated pH does not represent well the observed decrease from seafloor to the boundary between Units I and II, but it represents relatively well the downward pH increase with maxima in Unit III. The simulated inflection of porewater strontium agrees well with observations, but simulated maxima at 275 mbsf overestimates observed maxima by a factor of 1.3 times. Dissolved silica has the largest discrepancies with the calculated values trending opposite to the observations throughout the simulated sedimentary column. The computed low concentration of dissolved silica until 400 mbsf is due to the simulated formation of authigenic clinoptilolite, smectite and chlorite. The slightly higher computed porewater silica from 600 to 1,400 mbsf is due to the more extensive volcanic ash dissolution computed in the numerical model at this depth, and the lower computed amount of authigenic smectite and chlorite. The discrepancies between simulated and observed porewater silica from 600 to 1,400 mbsf may be due to an incomplete representation of the silica-containing authigenic mineral phases in the numerical model,

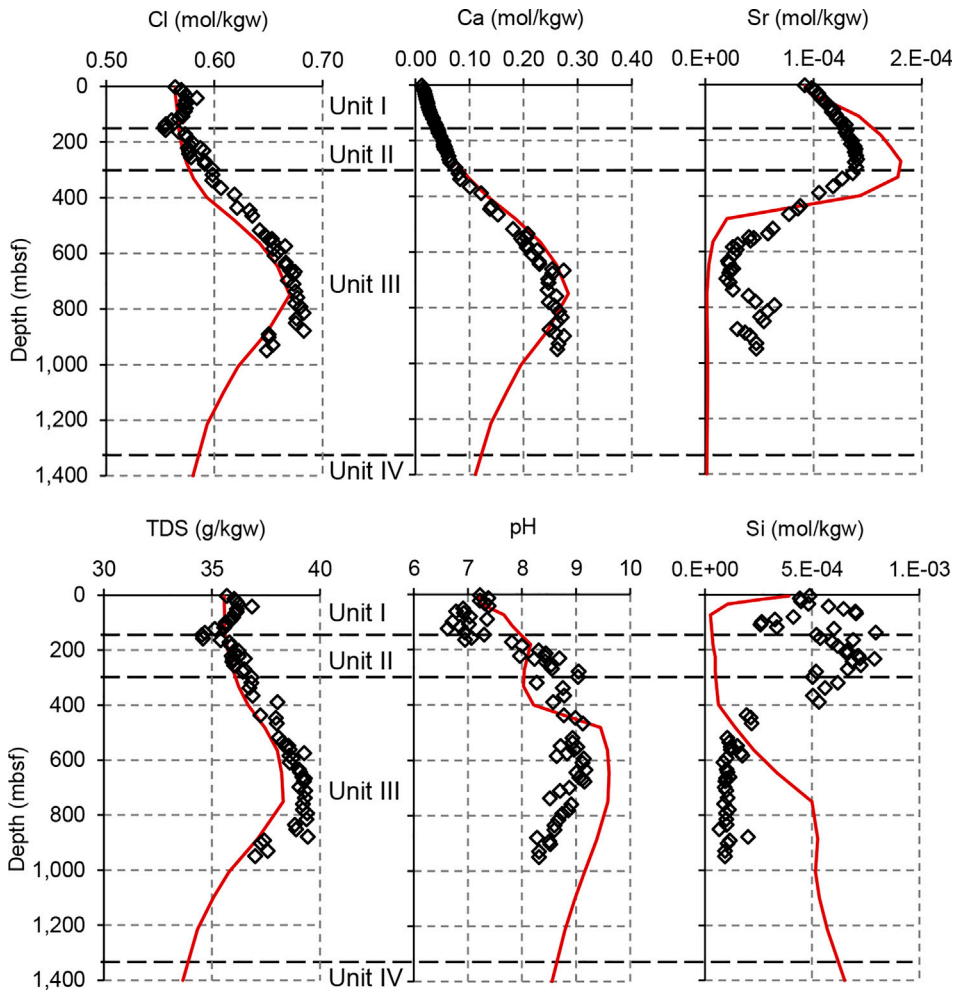

FIGURE 7
Comparison between observed (open diamond) and simulated (red line) porewater depth profiles of chloride, calcium, strontium, TDS (Total Dissolved Solids calculated in PHREEQC with observed porewater data), pH and silica. Total depth of the simulation corresponds to that of the sedimentary basin.

which would lower the simulated concentration of porewater silica, and therefore improve the fit between observed and simulated data. Minerals such as saponite, pyrophyllite and amesite are strong candidates for these silica-containing authigenic minerals (Aagaard and Jahren, 1992; and Arculus et al., 2015b). We tried including these mineral phases in the numerical model but numerical convergence issues forced us to withdraw from this option.

As mentioned in section 2, measured porewater data were used in the objective function of the parameter estimation performed with PEST (Doherty, 2005) to estimate the geochemical reaction constraints. Therefore, the plots shown in Figure 7 (and in Supplementary Material S2, for the remaining porewater data) reflect the goodness of fit of this calibration. Contrary to the porewater data, the observed amount of minerals and volcanic ash were not included in the calibration of the numerical model, and therefore can be used to check showing how well the numerical model represents observed solid phase data (Figure 8).

Observed volcanic ash content is around 25 wt% in Unit I. In Units II and III, it shows considerable scatter, reaching a maximum of 80 wt% at 390 mbsf, and a minimum of 0 wt% between 858 and 883 mbsf (Figure 8). The simulated volcanic ash content agrees with observed data in Unit I, and it is within the observed range in Units II and III. The location of the simulated minimum volcanic ash content coincides with observed minima, between 700 and 900 mbsf. The XRD-estimated amount of anorthite also shows considerable scatter and the simulated anorthite amount falls within the observed range.

The XRD-estimated amount of clinoptilolite is below 2 wt% in Unit I, below 3 wt% in Unit II, and scattered between <2 wt% and 9 wt% in Unit III, the maxima being located between 548 and

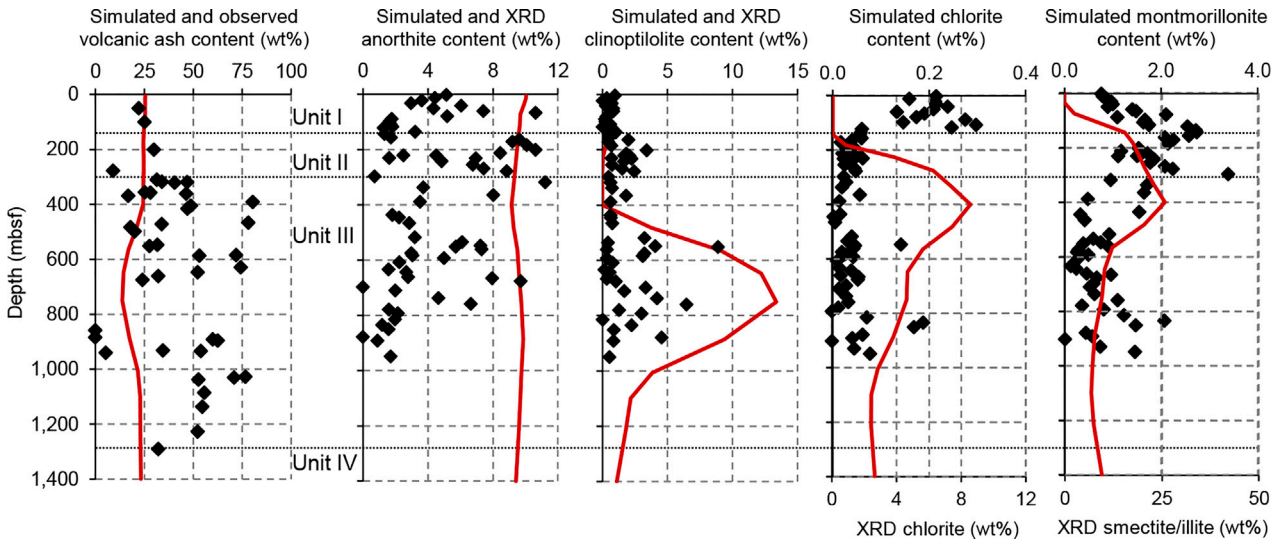

FIGURE 8
Simulated depth profiles of the relative amount of volcanic ash, anorthite, clinoptilolite, chlorite (clinochlore 14A), and smectite (red lines). Observed vitric content (expressed in weight percent), and XRD-estimated content of anorthite, clinoptilolite, chlorite and smectite, corrected for the observed vitric content (black diamonds). Note the different scales for XRD-estimated and simulated amount of chlorite and smectite/illite.

759 mbsf (Figure 8). The simulated amount of clinoptilolite agrees relatively well with the observed trends. The XRD-estimated amount of chlorite and smectite/illite (maxima of 9 and 42 wt%, respectively) is much higher than the values predicted in the numerical simulation (maxima of 0.3 and 0.2 wt%, respectively). This could indicate that part of the XRD-estimated amount of chlorite and smectite/illite is detrital, while the numerically computed amount of chlorite and smectite refers to the authigenic fraction. How much of the XRD-estimated amount of these minerals is detrital is still unknown, but the isotopic strontium composition of the two topmost bulk sediment samples enriched in radiogenic ^{87}Sr indicate a clear contribution from continental rocks (Figure 3).

Discussion

Extent of volcanic ash diagenesis and implications for the isotopic signature of dissolved strontium ($^{87}Sr/^{86}Sr$)

The lowest volcanic ash content, revealed by observed data (Figure 4), occurs at the bottom of Unit II (277 mbsf), and between 670 and 940 mbsf, in Unit III. A relatively high concentration of measured dissolved silica (7×10^{-4} mol/L) coincides with the low ash content at the bottom of Unit II. In Unit III, the intense formation of authigenic zeolites (up to 70 wt%, according to XRD data), smectite/illite (up to 26 wt%) and chlorite (up to 6 wt%) has consumed most of the dissolved silica, indicating that between 670 and 940 mbsf, ash diagenesis has been most prominent.

Due to the inherent difficulty in assessing its actual value, the initial amount of volcanic ash contained in the sediment when it settles at the sea bottom is assumed 25 wt% during the entire simulation period for the reaction-diffusion numerical model of the ASB. Therefore, the quantitative estimation of the extent of volcanic ash diagenesis, based on the outputs of the numerical model, is subject to this uncertainty. The numerical simulation of 47.8 million years of sediment accumulation and volcanic ash diagenesis in the ASB indicates that up to 11 wt% of volcanic ash is dissolved in Unit III, at 750 mbsf. This corresponds to 45% of the initial amount of volcanic ash being dissolved after 34 Ma of sediment accumulation and diagenesis. The maximum dissolved amount of volcanic ash computed in the other lithological units is <1 wt% in Unit I, 1 wt% in Unit II, and 2 wt% in Unit IV (for more details see section 1.2.3, in Supplementary Material S2). The much higher extent of volcanic ash diagenesis computed in Unit III coincides with the period of high sedimentation rate that occurred from 36 to 28 Ma (Figure 1). These numerical modelling results are interpreted as follows: during a period of higher sedimentation rate the amount of fresh volcanic ash accumulated and put in contact with seawater for a given time interval is higher than in periods of lower sedimentation rate. Since the kinetic dissolution rate of volcanic ash is directly proportional to the amount of volcanic ash in the sediment, periods with high sedimentation rate will experience a more pronounced volcanic ash dissolution. In addition, the

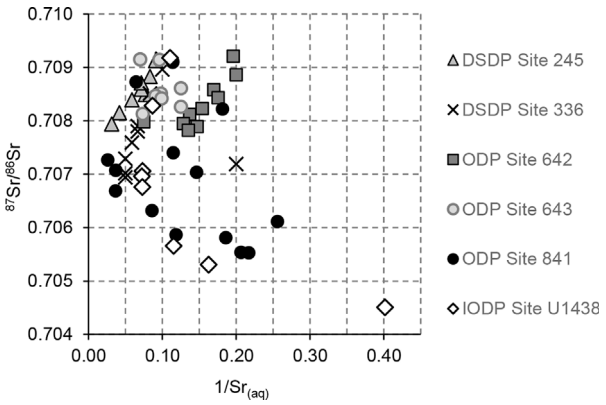

FIGURE 9
Comparison of the porewater $^{87}Sr/^{86}Sr$ versus $1/Sr_{(aq)}$ in the IODP Site U1438 with other deep-sea drilling sites; Madagascar Basin (DSDP Site 245; Hawkesworth and Elderfield, 1978), Iceland-Faeroe Ridge (DSDP Site 336; Hawkesworth and Elderfield, 1978), Tonga Fore-arc (ODP Site 841; Blanc et al., 1995), and the Vøring Plateau (ODP Sites 642 and 643; Aagaard et al., 1989).

temperature and pressure at these depths lead to increased solubility of amorphous silica (see Figure 3) which makes volcanic ash thermodynamically more vulnerable to dissolution.

When volcanic ash dissolves an isotopically less radiogenic strontium (lower $^{87}Sr/^{86}Sr$) is released into the porewater relative to contemporary seawater. This is clearly seen in Figure 3 where the porewater strontium is much less radiogenic than the contemporary seawater in all except the topmost sample. The contribution of volcanic minerals and ash dissolution to dissolved strontium could be up to 78 and 100%, at 737 and 518 mbsf, respectively. The less radiogenic strontium is characteristic of the volcanic ash and minerals deposited in the ASB, with a bulk sediment value of 0.7036, at 737 mbsf. The two topmost bulk sediment samples, on the contrary, show the most radiogenic isotopic signature (0.7131–0.7143) indicating a clear contribution from sediments rich in radiogenic ^{87}Sr originated from the Asian continent (Jiang et al., 2013).

In Figure 9, the porewater $^{87}Sr/^{86}Sr$ data obtained at IODP Site U1438 is plotted against $1/Sr_{(aq)}$ (the inverse of the concentration of aqueous strontium) together with data from four other locations where volcaniclastic-rich sediments were recovered: the west Indian Ocean (DSDP Site 245 in the Madagascar Basin; Hawkesworth and Elderfield, 1978); two locations in the north Atlantic Ocean (DSDP Site 336 in the Iceland-Faeroe Ridge; Hawkesworth and Elderfield, 1978; and the ODP Sites 642 and 643 in the Vøring Plateau; Aagaard et al., 1989); and, the west Pacific Ocean (ODP Site 841 in the Tonga Fore-arc; Blanc et al., 1995). The extremely low porewater $^{87}Sr/^{86}Sr$ observed at IODP Site U1438 indicates that the dissolution of volcanic minerals and ash has contributed more remarkably to the isotopic composition of porewater strontium than in any of the other Sites. In addition, at values of $1/Sr_{(aq)}$ higher than 0.10, IODP Site U1438 and ODP Site 841 behave similarly; with the isotopic signature of strontium decreasing as the concentration of dissolved strontium decreases (i.e., as $1/Sr_{(aq)}$ increases).

Origin of the deep calcium chloride brine

The deep $CaCl_2$ brine, that is, observed below 600 mbsf in the ASB is well represented in the reaction-diffusion numerical model developed here, as shown in Figure 7. The formation of this brine can therefore be explained based on the outputs of the numerical model and subsequent mass balance calculations performed for water (H_2O), chloride (Cl^-) and calcium (Ca^{2+}).

The porewater chloride profile computed in the reaction-diffusion model (previously shown in Figure 7) is plotted in Figure 10 under the label *WRI+ECM* (water-rock interactions coupled to electrochemical migration of solutes) together with other porewater chloride profiles that depict the prevailing hydrogeochemical process in each part of the profile. The other chloride profiles shown in Figure 10 were calculated from the initial porewater chloride concentration (i.e., the concentration prior to diagenesis), and either adding chloride in line with the computed mass of dissolved volcanic ash or, by removing H_2O from the porewater in line with the computed mass of hydrated authigenic secondary minerals at the end of the 48.7 million years of sediment accumulation and diagenesis in the ASB. Therefore, the curves labelled with these two processes (addition of Cl^- or removal of H_2O) reflect purely water-rock interactions (WRI), without the influence of electrochemical migration of solutes in the aqueous solution that fills-up the pore space. The corresponding calculations are given in section 1.2.4, in Supplementary Material S2.

The sum of all water-rock interactions (*Sum of all WRI*) is also shown in Figure 10, and because solute diffusion may add or remove chloride through the top boundary condition of the modelled sedimentary column (that represents the seafloor), the total mass of porewater chloride computed in the curve *Sum of all WRI* was compared with that obtained for *WRI+ECM*. Our calculations show a surplus of 0.5% in the *WRI+ECM* compared to the *Sum of all WRI* which could be an evidence of uphill diffusion of chloride into the sediment column, at the seafloor boundary. Uphill diffusion is the diffusive movement of a solute in the opposite direction of its concentration gradient driven by the electrochemical migration of solutes in the pore space.

Where volcanic ash diagenesis has been most prominent (600–1,000 mbsf), volcanic ash dissolution and formation of zeolites are the dominant processes contributing to the high

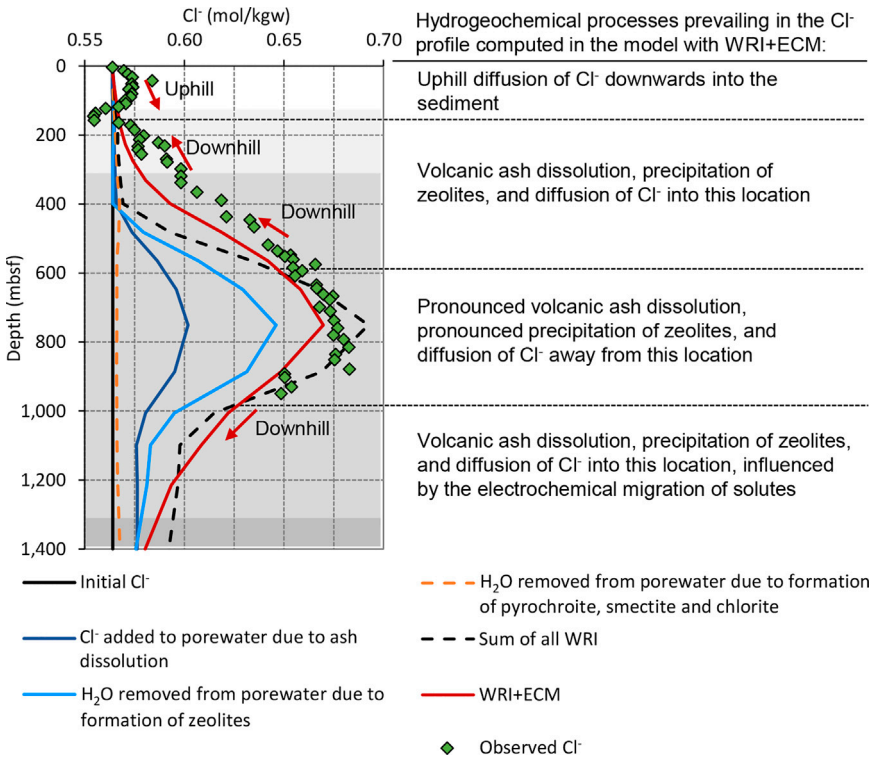

FIGURE 10
Identification of the hydrogeochemical processes prevailing in the different parts of the chloride profile computed in the reaction-diffusion model that couples water-rock interactions to electrochemical migration of solutes (WRI+ECM). The graded grey background indicates the four lithological units shown in Figure 1.

chloride concentration (dark and light blue lines in Figure 10, respectively). At this depth, a maximum of 13% of the initial H_2O in the pore space is estimated to be removed after 36 Ma of diagenesis, and the formation of zeolites accounts for 97% of this H_2O loss. For the whole sedimentary column, the chloride added to the porewater via ash dissolution represents only 2% of the total porewater chloride observed nowadays.

When all the water-rock interactions are summed up (dashed black line in Figure 10), a higher concentration of chloride is calculated at 600 to 1,000 mbsf and below 1,200 mbsf than that which is predicted in the reaction-diffusion model (*WRI+ECM* in Figure 10). In line with the *WRI+ECM* curve, chloride has moved away from these locations through diffusion in the pore space. The diffusion of chloride in these locations is in the direction of the concentration gradient, i.e. downhill diffusion, but strongly diminished by the electrochemical migration of solutes. In the upper part of the profile (until 160 mbsf), the electrochemical migration of solutes cause chloride to move downward in the sediment column in the opposite direction of the concentration gradient, i.e., uphill diffusion, sustaining the downward diffusion of seawater chloride into the sediments.

At ODP Site 793 in the Izu-Bonin fore-arc, a similar lithology to the ASB was recovered down to a depth of 1,682 mbsf. Here, Egeberg et al. (1990) estimated a removal of ~26% of the H_2O from the pore space due to the formation of authigenic minerals, based exclusively on the observed high concentration of porewater chloride. These authors did not take into account the effects of the electrochemical migration of chloride nor the contribution of volcanic ash dissolution to the observed porewater chloride, and this could be the reason why we estimate a lower removal of H_2O from the pore space of 13%, based on the outputs of the reaction-diffusion numerical model developed for the ASB.

As for chloride, we also depict the prevailing hydrogeochemical processes in the different parts of the porewater calcium profile computed in the reaction-diffusion model (*WRI+ECM* in Figure 11). Calcium becomes the dominant cation in porewater at 666 mbsf, coinciding with the upper part of the section where volcanic ash diagenesis has been most prominent (600–1,000 mbsf). Anorthite dissolution has contributed the most to the porewater enrichment in calcium (green line in Figure 11). For the whole sedimentary column, the calcium added to porewater via anorthite dissolution represents 41%

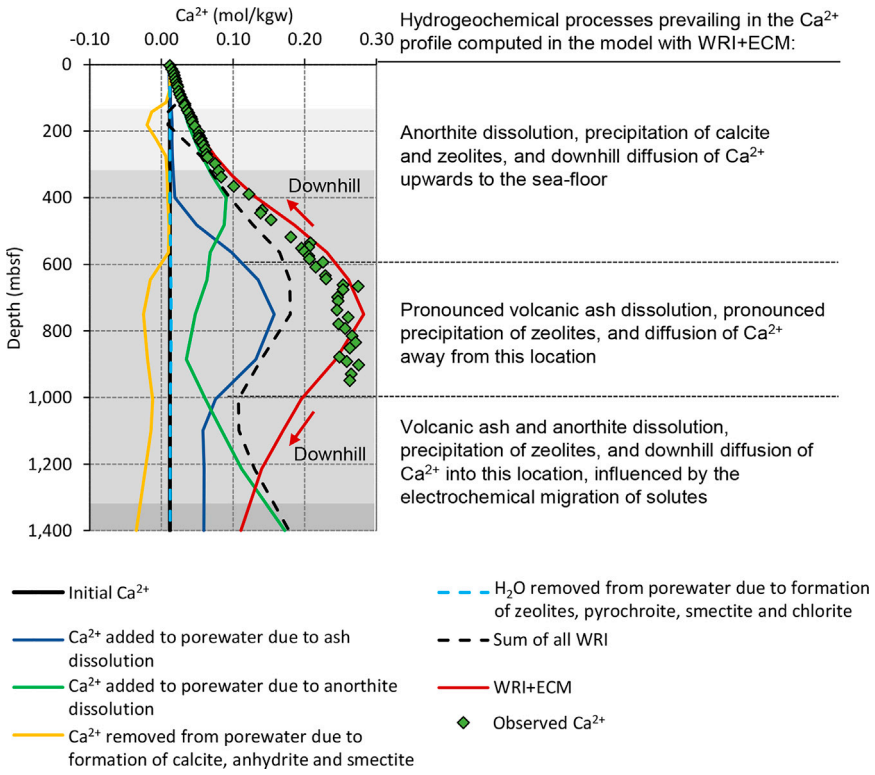

FIGURE 11
Identification of the hydrogeochemical processes prevailing in the different parts of the calcium profile computed in the reaction-diffusion model that couples water-rock interactions to electrochemical migration of solutes (WRI+ECM). The graded grey background indicates the four lithological units shown in Figure 1.

of the total porewater calcium observed nowadays, and ash dissolution contributes 33%. In addition, the comparison between the curves *Sum of all WRI* and *WRI+ECM* indicates that diffusion of calcium in the pore space occurs downhill along its concentration gradient but it is hindered by the electrochemical migration of solutes.

Conclusion

The 1,461 m-thick volcaniclastic sedimentary sequence accumulated in the ASB records the history of 48.7 million years of sediment accumulation and volcanic ash diagenesis. The sediment and porewater samples recovered from IODP Site U1438 provided a unique hydrogeochemical, microbiological and petrophysical dataset that motivated us to develop a reaction-diffusion numerical model that simulates the build-up of the sedimentary column and the water-rock interactions during this long-term diagenetic evolution.

From the seafloor to 800 mbsf, the concentration of porewater chloride increases 1.2 times, calcium increases 23 times, and sodium decreases 0.26 times. The isotopic signature of dissolved strontium reveals a downward increasing imprint from volcanic ash dissolution, and from 400 to 600 mbsf the isotopic signature of contemporary seawater is completely lost.

The observed ash content is on average 24, 27, and 36 wt% in the lithostratigraphic Units I, II and III, respectively. The main authigenic secondary minerals revealed by XRD and thin section analysis are smectite/illite clays in Unit II (up to 42 wt%) and zeolites in Unit III (up to 70 wt%).

The microbiological analyses reveal that bacterial and archaeal 16S gene abundances are highest in the upper 7 m of the sedimentary column. The Nitrosopumilales Archaea is predominant at the sediment-water interface, and below 50 mbsf Thermoplasmata become dominant. Relatively abundant Methanobacteria (97%) at 90 mbsf reveal some, but limited, methanogenic activity in the ASB. The porewater manganese inflections observed in Unit I may reflect the activity of prokaryotes that use Mn(IV)-oxides as an electron acceptor, and the archaeal phylum Woesearchaeota, abundant at 3 mbsf, could be a candidate for this process.

The reaction-diffusion numerical model developed with PHREEQC indicates that 45% of the initial amount of volcanic ash has been dissolved in Unit III, at 750 mbsf.

The amount of volcanic ash predicted to have dissolved in the whole sedimentary column contributes to only 2% of the porewater chloride observed. For porewater calcium, anorthite and volcanic ash dissolution contribute 41 and 33%, respectively.

The formation of the $CaCl_2$ brine in the Amami-Sankaku Basin is explained as follows. Where volcanic ash diagenesis has been most prominent (600–1,000 mbsf), 13% of the initial water (H_2O) in the pore space is estimated to have been removed, and the formation of zeolites accounts for 97% of this water loss. This loss of water is the main hydrogeochemical process leading to the high concentration of porewater chloride at this depth. For calcium, in contrast, anorthite and volcanic ash dissolution are the predominant processes. In addition, the mobility of calcium in the pore space is driven solely by downhill diffusion, while chloride shows a clear uphill diffusion that can only occur when solutes experience electrochemical migration.

Data availability statement

The IODP Expedition 351 dataset used for this study can be found in the IODP Repository https://web.iodp.tamu.edu/LORE/. The additional post-cruise data used in this work is available as Supplementary Material.

Author contributions

All co-authors contributed to the conceptualization and writing, and approved the submitted version of this manuscript. In addition, CS, DP, CV, FC, VO, and ML contributed to the methodology and investigation. CS, FT, FJ, FC, VO, and ML contributed to the resources and data curation. DP contributed to the software development and programming.

Funding

Thanks are due to FCT/MCTES for the financial support to CESAM (UIDP/50017/2020+UIDB/50017/2020+LA/P/0094/2020), through national funds. CS thanks the Akademia grant awarded to the University of Oslo, FCT through the Grant BPD/87102/2012, IODP Portugal and the ECORD Research Grant that funded the work at the Stable Isotope Laboratory in the University of Salamanca. VO was funded by National funds (OE), through FCT, in the scope of the framework contract foreseen in the numbers 4, 5 and 6 of the article 23, of the Decree-Law 57/2016, of August 29, changed by Law 57/2017, of July 19. VO's work-visit to ETH Zurich was funded by the e-Cost Action FLOWS. FJRCC was funded by national funds through FCT under the Scientific Employment Stimulus—Individual Call—reference CEECIND/00070/2017.

Acknowledgments

The authors thank the IODP shipboard scientists and staff of Expedition 351, and the JOIDES Resolution crew. Excellent conditions were given by IODP for the preparation and shipment of the sediment samples for post-cruise microbiological analyses. Rosario Soares and Beyene Haile are acknowledged for guidance on the interpretation of XRD data, and Sara Ribeiro for the strontium isotopes analyses. Special thanks go to Luis Menezes Pinheiro for valuable advices, Richard Webb for the guidance on the PEST simulations, and Anthony Appelo for valuable comments to the PHREEQC simulations. We thank Per Aagaard and two reviewers whose comments greatly contributed to improve this manuscript.

Conflict of interest

The authors declare that the research was conducted in the absence of any commercial or financial relationships that could be construed as a potential conflict of interest.

Publisher's note

Supplementary material

The Supplementary Material for this article can be found online at: https://www.frontiersin.org/articles/10.3389/feart.2022.869567/full#supplementary-material

SUPPLEMENTARY MATERIAL S1
Sample_prep_and_analyses.docx

SUPPLEMENTARY MATERIAL S1
MBIO_sample_location_time.tsv

SUPPLEMENTARY MATERIAL S1
MBIO_Arch_classes.tsv

SUPPLEMENTARY MATERIAL S1
MBIO_Bact_orders.tsv

SUPPLEMENTARY MATERIAL S1
MBIO_Bacteria_Archaea_copy_nr.tsv

SUPPLEMENTARY MATERIAL S1
XRD-plots.pdf

SUPPLEMENTARY MATERIAL S1
XRD-plots_sample_ref_depth.tsv

SUPPLEMENTARY MATERIAL S2
PHREEQC_PEST_models.docx.
The PHREEQC input and output files created for the aqueous speciation calculations of the porewaters sampled in IODP Site U1438 are described in section 1.1 of the file S2.PHREEQC_PEST_models.docx, and are available in the compressed folder in-situ_P-T.zip. In this compressed folder, the file "IODP351_U1438_porewater_data.xlsx" contains the porewater data (sheet "LIMS_database_U1438") as produced onboard JOIDES (retrievable from https://web.iodp.tamu.edu/LORE/), and the input porewater data after performing aqueous speciation of this porewater data for in-situ pressure and temperature (sheet "PHREEQC_input_in-situ_P-T"). The PHREEQC and PEST input and output files created for the reaction-diffusion numerical model of the Amami-Sankaku Basin are described in section 1.2 of the file S2.PHREEQC_PEST_models.docx, and are available in the compressed folder reac-diff-model.zip.

References

Aagaard, P., Egerberg, P. K., and Smalley, P. C. (1989). "Diagenetic Reactions in Leg 104 Sediments Inferred from Isotope and Major Element Chemistry of Interstitial Waters,". O. Eldholm, J. Thiede, E. Taylor, et al.,104, 273–280.*Proc. Ocean Drill. Program, Sci. Results*

Aagaard, P., and Jahren, J. S. (1992). Diagenetic Illite-Chlorite Assemblages in Arenites. II. Thermodynamic Relations. *Clays Clay Min.* 40 (5), 547–554. doi:10.1346/ccmn.1992.0400508

Arculus, R. J., Ishizuka, O., Bogus, K. A., Gurnis, M., Hickey-Vargas, R., Aljahdali, M. H., et al. (2015b). A Record of Spontaneous Subduction Initiation in the Izu-Bonin-Mariana Arc. *Nat. Geosci.* 8, 728–733. doi:10.1038/ngeo2515

Arculus, R. J., Ishizuka, O., Bogus, K., Aljahdali, M. H., Bandini-Maeder, A. N., Barth, A. P., et al. (2015a). "Site Report U1438," in *Expedition Izu–Bonin–Mariana Arc Origins Proceedings of the International Ocean Discovery Program 351*. Editors R. J. Arculus, O. Ishizuka, and K. A. Bogus.

Blanc, G., Vitali, F., and Stille, P. (1995). Unusual Diagenetic Alteration of Volcanoclastic Sediments in the Tonga Fore-Are: Evidence from Chemical and Strontium Isotopic Compositions of Interstitial Waters. *Geochim. Cosmochim. Acta* 59 (22), 4633–4644. doi:10.1016/0016-7037(95)00317-7

Blöthe, M., Wegorzewski, A., Müller, C., Simon, F., Kuhn, T., and Schippers, A. (2015). Manganese-Cycling Microbial Communities inside Deep-Sea Manganese Nodules. *Environ. Sci. Technol.* 49, 7692–7700. doi:10.1021/es504930v

Boudreau, B. P., Meysman, F. J. R., and Middelburg, J. J. (2004). Multicomponent Ionic Diffusion in Porewaters: Coulombic Effects Revisited. *Earth Planet. Sci. Lett.* 222 (2), 653–666. doi:10.1016/j.epsl.2004.02.034

Brandl, P., Hamada, M., Arculus, R. J., Johnson, K., Marsaglia, K. M., Savov, I. P., et al. (2017). The Arc Arises: the Links between Volcanic Output, Arc Evolution and Melt Composition. *Earth Planet. Sci. Lett.* 461, 73–84. doi:10.1016/j.epsl.2016.12.027

Carpenter, A. B. (1978). Origin and Chemical Evolution of Brines in Sedimentary Basins. *Okla. Geol. Surv. Circ.* 79, 60–77.

Cosgrove, M. E., and Papavassiliou, C. T. (1979). Clinoptilolite in DSDP Sediments of the Indian Ocean (Site 223, Leg 23): Its Stability Conditions and Estimation of its Free Energy. *Mar. Geol.* 33 (3–4), 77–84. doi:10.1016/0025-3227(79)90075-6

D'Hondt, S., Jørgensen, B. B., Miller, D. J., Batzke, A., Blake, R., Cragg, B. A., et al. (2004). Distributions of Microbial Activities in Deep Subseafloor Sediments. *Science* 306, 2216–2221. doi:10.1126/science.1101155

Döbelin, N. (2021). Profex User Manual. Part 2: Using Profex. Version 4.3. Available at https://www.profex-xrd.org (Accessed June 01, 2021).

Doherty, J. (2005). "PEST – Model-independent Parameter Estimation," in *Watermark Numerical Computing*. 5th Edition.

Durbin, A. M., and Teske, A. (2011). Microbial Diversity and Stratification of South Pacific Abyssal Marine Sediments. *Environ. Microbiol.* 13 (12), 3219–3234. doi:10.1111/j.1462-2920.2011.02544.x

Egeberg, P. K., Fujioka, K., Taylor, B., Janecek, T., Aitchison, J., Cisewski, S., et al. (1990). Unusual Composition of Pore Waters Found in the Izu-Bonin Fore-Arc Sedimentary Basin. *Nature* 344 (6263), 215–218. doi:10.1038/344215a0

Gavrieli, I., Starinsky, A., Spiro, B., Aizenshtat, Z., and Nielsen, H. (1995). Mechanisms of Sulfate Removal from Subsurface Calcium Chloride Brines: Heletz-Kokhav Oilfields, Israel. *Geochim. Cosmochim. Acta* 59 (17), 3525–3533. doi:10.1016/0016-7037(95)00229-S

Gieskes, J. M., Blanc, G., Vrolijk, P., Elderfield, H., and Barnes, R. (1990). "Interstitial Water Chemistry – Major Constituents," in *Proceedings of the Ocean Drilling Program, Scientific Results*. Editors J. C. Moore and A. Mascle.

Gieskes, J. M., Gamo, T., and Brumsack, H. (1991). *Chemical Methods for Interstitial Water Analysis Aboard JOIDES Resolution*.

Gieskes, J. M., and Lawrence, J. R. (1981). Alteration of Volcanic Matter in Deep Sea Sediments: Evidence from the Chemical Composition of Interstitial Waters from Deep Sea Drilling Cores. *Geochim. Cosmochim. Acta* 45 (10), 1687–1703. doi:10.1016/0016-7037(81)90004-1

Hanshaw, B. B., and Coplen, T. B. (1973). Ultrafiltration by a Compacted Clay Membrane—II. Sodium Ion Exclusion at Various Ionic Strengths. *Geochim. Cosmochim. Acta* 37 (10), 2311–2327. doi:10.1016/0016-7037(73)90106-3

Hardie, L. A. (1983). Origin of $CaCl_2$ Brines by Basalt-Seawater Interaction: Insights provided by Some Simple Mass Balance Calculations. *Contr. Mineral. Pet.* 82 (2-3), 205–213. doi:10.1007/BF01166615

Hawkesworth, C. J., and Elderfield, H. (1978). The Strontium Isotopic Composition of Interstitial Waters from Sites 245 and 336 of the Deep Sea Drilling Project. *Earth Planet. Sci. Lett.* 40 (3), 423–432. doi:10.1016/0012-821X(78)90165-6

Ishizuka, O., Hickey-Vargas, M., Arculus, R. J., Yogodzinski, G. M., Savov, I. P., et al. (2018). Age of Izu–Bonin–Mariana Arc Basement. *Earth Planet. Sci. Lett.* 481, 80–90. doi:10.1016/j.epsl.2017.10.023

Jiang, F., Frank, M., Li, T., Chen, T.-Y., Xu, Z., and Li, A. (2013). Asian Dust Input in the Western Philippine Sea: Evidence from Radiogenic Sr and Nd Isotopes. *Geochem. Geophys. Geosyst.* 14 (5), 1538–1551. doi:10.1002/ggge.20116

Johnson, K., Marsaglia, K. M., Brandl, P. A., Barth, A. P., Waldman, R., Ishizuka, O., et al. (2021). Intra-oceanic Submarine Arc Evolution Recorded in an ~1-Km-Thick Rear-Arc Succession of Distal Volcaniclastic Lobe Deposits. *Geosph. (Boulder).* 17 (4), 957–980. doi:10.1130/GES02321.1

Jungluth, S. P., Johnson, L. G. H., Cowen, J. P., and Rappé, M. S. (2013). "Data Report: Microbial Diversity in Sediment Near Grizzly Bare Seamount in Holes U1363B and U1363G," in *The Expedition 327 Scientists, Proc. IODP*. Editors A. T. Fisher, T. Tsuji, and K. Petronotis (Tokyo: Integrated Ocean Drilling Program Management International, Inc). doi:10.2204/iodp.proc.327.201.201

Katz, A., and Starinsky, A. (2008). Geochemical History of the Dead Sea. *Aquat. Geochem.* 15 (1-2), 159–194. doi:10.1007/s10498-008-9045-0

Kharaka, Y. K., and Berry, F. A. (1973). Simultaneous Flow of Water and Solutes through Geological Membranes—I. Experimental Investigation. *Geochim. Cosmochim. Acta* 37 (12), 2577–2603. doi:10.1016/0016-7037(73)90267-6

Kusano, Y., Ishizuka, O., Hickey-Vargas, R., and Arculus, R. J. (2021). Emplacement Processes of Proto-Arc Basalt in the Izu-Bonin-Mariana Arc System. *Isl. Arc* 30 (1), 1–16. doi:10.1111/iar.12401

Lanoil, B. D., Duc, M. T. L., Wright, M., Kastner, M., Nealson, K. H., and Bartlett, D. (2005). Archaeal Diversity in ODP Legacy Borehole 892b and Associated Seawater and Sediments of the Cascadia Margin. *FEMS Microbiol. Ecol.* 54, 167–177. doi:10.1016/j.femsec.2005.03.015

Lee, Y. I., and Klein, G. D. (2003). "Diagenesis of Sandstones in the Back-Arc Basins of the Western Pacific Ocean," in *Sandstone Diagenesis: Recent and Ancient*. Editors Burley and Worden.

Lever, M. A., Torti, A., Eickenbusch, P., Michaud, A. B., Šantl-Temkiv, T., and Jørgensen, B. B. (2015). A Modular Method for the Extraction of DNA and RNA, and the Separation of DNA Pools from Diverse Environmental Sample Types. *Front. Microbiol.* 6, 476. doi:10.3389/fmicb.2015.00476

Li, H., Arculus, R., Ishizuka, O., Hickey-Vargas, R., Yogodzinski, G. M., McCarthy, A., et al. (2021). Basalt Derived from Highly Refractory Mantle Sources during Early Izu-Bonin-Mariana Arc Development. *Nat. Commun.* 12 (1), 1723. doi:10.1038/s41467-021-21980-0

Liu, X., Li, M., Castelle, C. J., Probst, A. J., Zhou, Z., Pan, J., et al. (2018). Insights into the Ecology, Evolution, and Metabolism of the Widespread Woesearchaeotal Lineages. *Microbiome* 6, 102. doi:10.1186/s40168-018-0488-2

Lowenstein, T. K., and Risacher, F. (2008). Closed Basin Brine Evolution and the Influence of Ca–Cl Inflow Waters: Death Valley and Bristol Dry Lake California, Qaidam Basin, China, and Salar de Atacama, Chile. *Aquat. Geochem.* 15 (1-2), 71–94. doi:10.1007/s10498-008-9046-z

Maffione, M., and Morris, A. (2017). The Onset of Fabric Development in Deep Marine Sediments. *Earth Planet. Sci. Lett.* 474, 32–39. doi:10.1016/j.epsl.2017.06.018

Martin, J. B. (1994). "Diagenesis and Hydrology at the New Hebrides Forearc and Intra-arc Aoba Basin," in *Proc. Ocean Drilling Program*. Editors, et al.

Martin, J. B., Kastner, M., and Egeberg, P. K. (1995). "Origin of Saline Fluids at Convergent Margins," in *Active Margins and Marginal Basins of the Western Pacific. Geophysical Monograph Series*. Editors B. Taylor and J. Natland.

McArthur, J. M., Howarth, R. J., and Bailey, T. R. (2001). Strontium Isotope Stratigraphy: LOWESS Version 3: Best Fit to the Marine Sr-Isotope Curve for 0–509 Ma and Accompanying Look-Up Table for Deriving Numerical Age. *J. Geol.* 109, 155–170. doi:10.1086/319243

McCarthy, A., Yogodzinski, G. M., Bizimis, M., Savov, I. P., Hickey-Vargas, R., Arculus, R., et al. (2021). Volcaniclastic Sandstones Record the Influence of Subducted Pacific MORB on Magmatism at the Early Izu-Bonin Arc. *Geochim. Cosmochim. Acta* 296, 170–188. doi:10.1016/j.gca.2021.01.006

McCarthy, A., Yogodzinski, G. M., Tepley, F. J., III, Bizimis, M., Arculus, R., and Ishizuka, O. (2019). Isotopic Characteristics of Neogene-Quaternary Tephra from IODP Site U1438: A Record of Explosive Volcanic Activity in the Kyushu-Ryukyu Arc. *Geochem. Geophys. Geosyst.* 20, 2019GC008267–2333. doi:10.1029/2019GC008267

McDuff, R. E., and Gieskes, J. M. (1976). Calcium and Magnesium Profiles in DSDP Interstitial Waters: Diffusion or Reaction? *Earth Planet. Sci. Lett.* 33 (1), 1–10. doi:10.1016/0012-821X(76)90151-5

Murray, R. W., Miller, D. J., and Kryc, K. A. (2000). Analysis of Major and Trace Elements in Rocks, Sediments, and Interstitial Waters by Inductively Coupled Plasma–Atomic Emission Spectrometry (ICP-AES). *Odp. Tech. Note* 29. doi:10.2973/odp.tn.29.2000

Palandri, J. L., and Kharaka, Y. K. (2004). A Compilation of Rate Parameters of Water-Mineral Interaction Kinetics for Application to Geochemical Modeling. *U.S. Geol. Surv. Open File Rep. 2004* 1068, 64. doi:10.3133/ofr20041068

Parkes, J. R., Webster, G., Cragg, B. A., Weightman, A. J., Newberry, C. J., Ferdelman, T. G., et al. (2005). Deep Sub-seafloor Prokaryotes Stimulated at Interfaces over Geological Time. *Nature* 436, 390–394. doi:10.1038/nature03796

Parkhurst, D. L., and Appelo, C. A. J. (2013). *Description of Input and Examples for PHREEQC Version 3 – A Computer Program for Speciation, Batch-Reaction, One-Dimensional Transport, and Inverse Geochemical Calculations: U.S. Geological Survey Techniques and Methods*, 497. doi:10.3133/tm6A43

Rasouli, P., Steefel, C. I., Mayer, K. U., and Rolle, M. (2015). Benchmarks for Multicomponent Diffusion and Electrochemical Migration. *Comput. Geosci.* 19 (3), 523–533. doi:10.1007/s10596-015-9481-z

Schauer, R., Røy, H., Augustin, N., Gennerich, H. H., Peters, M., Wenzhoefer, F., et al. (2011). Bacterial Sulfur Cycling Shapes Microbial Communities in Surface Sediments of an Ultramafic Hydrothermal Vent Field. *Environ. Microbiol.* 13, 2633–2648. doi:10.1111/j.1462-2920.2011.02530.x

Sprocati, R., Masi, M., Muniruzzaman, M., and Rolle, M. (2019). Modeling Electrokinetic Transport and Biogeochemical Reactions in Porous Media: A Multidimensional Nernst–Planck–Poisson Approach with PHREEQC Coupling. *Adv. Water Resour.* 127, 134–147. doi:10.1016/j.advwatres.2019.03.011

Tsolis-Katagas, P., and Katagas, C. (1990). Zeolitic Diagenesis of Oligocene Pyroclastic Rocks of the Metaxades Area, Thrace, Greece. *Mineral. Mag.* 54 (374), 95–103. doi:10.1180/minmag.1990.054.374.10

Vitali, F., Blanc, G., and Larqué, P. (1995). Zeolite Distribution in Volcaniclastic Deep-Sea Sediments from the Tonga Trench Margin (SW Pacific). *Clays Clay Min.* 43 (1), 92–104. doi:10.1346/CCMN.1995.0430111

Waldman, R. J., Marsaglia, K. M., Hickey-Vargas, R., Ishizuka, O., Johnson, K. E., McCarthy, A., et al. (2021). Sedimentary and Volcanic Record of the Nascent Izu-Bonin-Mariana Arc from IODP Site U1438. *GSA Bull.* 133 (7-8), 1421–1440.

Wu, Y-H., Liao, L., Wang, C-S., Ma, W-L., Meng, F-X., Wu, M., et al. (2013). A Comparison of Microbial Communities in Deep-Sea Polymetallic Nodules and the Surrounding Sediments in the Pacific Ocean. *Deep Sea Res. Part I Oceanogr. Res. Pap.* 79, 40–49. doi:10.1016/j.dsr.2013.05.004